# Phase diagram of polydisperse Na-fluorohectorite–water suspensions: A synchrotron small-angle x-ray scattering study

D. M. Fonseca,[1,*] Y. Méheust,[1,2] J. O. Fossum,[1,†] K. D. Knudsen,[3] and K. P. S. Parmar[1,4]
[1]*Department of Physics, Norwegian University of Science and Technology (NTNU), Trondheim, Norway*
[2]*Geosciences Rennes, UMR CNRS 6118, Université de Rennes 1, Rennes, France*
[3]*Physics Department, Institute for Energy Technology (IFE), Kjeller, Norway*
[4]*Department of Chemical Engineering, Pohang University of Science and Technology, Pohang, South Korea*
(Received 6 August 2008; published 6 February 2009)

Systems of platelet-shaped nanostacks of the synthetic clay Na-fluorohectorite, suspended in saline solutions of various salt concentrations, exhibit a rich phase behavior with up to four phases coexisting in a single sample tube. They are studied here using small-angle x-ray scattering: the anisotropy of the obtained images is quantified, and, together with x-ray absorption measurements, this provides a precise determination of the phase boundaries, as well as a measure of the orientational ordering of the clay colloids in the various gel phases. The coexistence of different phases results from a sedimentation-induced vertical gradient in particle fraction. Quantitative relation of the vertical coordinate to the clay particle fraction in these samples allows determination of a phase diagram for these Na-fluorohectorite systems, as a function of the particle fraction and salt concentration.

DOI: 10.1103/PhysRevE.79.021402 PACS number(s): 82.70.Gg, 64.75.Xc, 61.05.cf

## I. INTRODUCTION

Liquid suspensions of clays have received special attention during recent years. This is due among other factors to their role as model systems for nanoparticle assembly and ordering, including long-range ordering phenomena. These clay systems are interesting both for industrial applications and from a basic science point of view. Industrial applications for clay minerals range from petroleum-relevant areas to food and cosmetics. Fundamental studies of the complex physical phenomena in clay systems, and the resulting applications, are far from complete. Being "abundant, inexpensive, and environment friendly," clays are recognized by some authors as "the materials of the 21st century" [1].

The fluorohectorite studied here is a smectite clay, characterized by a layer structure with a layer thickness in the nanometer range. The smectite clay layer consists of one aluminum octahedral layer between two silicon tetrahedral layers (2:1 layer unit). Such layers stack together, but owing to their negatively charged surfaces, intercalated cations such as $Na^+$ or $K^+$ are needed to balance the charge and allow their stacking (see Fig. 1). Furthermore, these particle stacks can swell in the presence of water, i.e., water molecules may enter the interlayer space, increasing the distance between layers [2].

The basic colloidal particles that we will be discussing in the present paper are stacks of such layers with counterions between them, which we will call a platelet. The thickness, diameter, and surface charge of the platelets vary according to the type of smectite clay. The extensively studied laponite [3–5], for instance, has a platelet consisting of one single 2:1 layer unit with a diameter of around 30 nm and thickness of 1 nm [6].

In the present work we study sodium fluorohectorite (NaFHT) which is a synthetic 2:1 clay mineral where $Na^+$ is the counterion in the interlayer space. NaFHT is characterized by a high surface charge, $1.2e^-$ per unit cell ($Si_8O_{20}$), and by its high polydispersity in both particle size and aspect ratio [7]: the platelets display diameters varying from around 100 nm to 20 $\mu$m, and the observed thickness is in the 30–150 nm range [8]. NaFHT-NaCl-$H_2O$ systems exhibit several coexisting phases which have been studied by x-ray diffraction [8], leading to the identification of three different gel phases characterized by differences in orientational order and/or size of the domains. Visual observations including the use of crossed polarizers [9] corroborated these wide-angle x-ray scattering measurements since a birefringent region was found coinciding with the oriented one. Recent studies include (i) magnetic resonance imaging (MRI) experiments of anisotropic water self-diffusion [10] which confirmed the isotropic-to-nematic transition and helped understand the orientation of the platelets; and (ii) small-angle x-ray scattering (SAXS) experiments [11] which attempted to obtain a fine characterization of the phase boundaries over a wide NaCl concentration range.

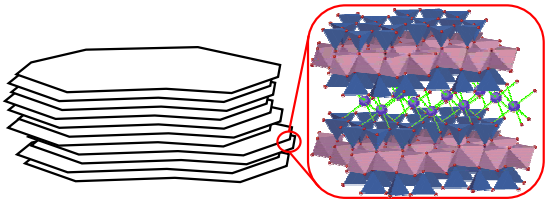

FIG. 1. (Color online) Simplified clay structure. The sodium fluorohectorite smectite clay particles are formed by stacked platelets with a thickness in the range 30–150 nm and a diameter in the range 100–20 000 nm. Detail: two platelets, each formed by an octahedral layer between two tetrahedral layers, and the counterions between them. For NaFHT the octahedra have Li and Mg and the tetrahedra are composed of Si; both structures have vertices of O and F, and the counterion is $Na^+$.

*fonseca@ntnu.no
†jon.fossum@ntnu.no

 

Saline solutions of NaFHT exhibit interesting phase behaviors owing to the competition between the van der Waals attraction and the electrostatic repulsion between the particles [12] and also due to the strong particle anisotropy. Since the electrostatic repulsion can be controlled by adding ions [13], systems of smectite clays in saline solutions are good systems for the study of self-assembly from platelet-shaped colloidal particles, including nematic self-assembly [3,5,14]. The particle anisotropy plays an important role as shown by Onsager [15], in his prediction that they undergo an isotropic-to-nematic transition at appropriate concentrations. Another interesting system is hard colloidal gibbsite platelets with an average diameter of 237 nm and thickness of 18 nm; this system was the first one shown to display isotropic, nematic, and columnar phases [16,17].

In this study, we employ the SAXS technique in order to study NaFHT dispersed in saline solutions. We attempt to obtain a proper phase diagram for the system, as determined by the volume fraction of clay and the concentration of sodium chloride. We also try to understand its organization from the profile of the SAXS patterns: at the selected range of x-ray scattering vectors, SAXS provides information on the arrangement regarding some of the dimensions of interest for our system, namely, the interparticle spacing and the thickness of the particles.

## II. EXPERIMENT

Li-fluorohectorite clay was purchased in powder form from Corning Inc. (New York). It was cation-exchanged using NaCl, and then dialyzed in order to remove the excess $Na^+$ and $Cl^-$ ions, and finally dried at 105 °C. The obtained clay crystallites have the nominal chemical formula $Na_{0.6}(Mg_{2.4}Li_{0.6})Si_4O_{10}F_2$. The samples were prepared though suspension of NaFHT in saline solutions at several concentrations; they are 3% NaFHT by mass and have the following NaCl concentrations: 0.1, 0.25, 0.5, 0.75, 1, 2.5, 5, 7.5, 10, and 25 m*M*. After their preparation they were left shaking for 12 h at 1000 rpm. Subsequently they were poured into 2 mm quartz capillaries until 7 cm of the capillaries were filled. The capillaries were then sealed with melted wax and left settling for 30 days. After a few days of settling, one can observe up to four phases in each capillary depending on the saline concentration [Figs. 2(a) and 2(b)]. The phase at the bottom is made of flocculated particles and is opaque; the one on top of it is translucent gel-like and is constituted of particles with a preferred direction of orientation; the next phase is transparent gel-like, created by particles without orientational ordering; and the phase at the top is transparent sol-like. In case the saline concentration is further increased—at some point—it will lead to total flocculation of the clay particles. It is worth mentioning that we here employ the word gel in a broad sense, since we could actually have a conventional gel, a glass, or both at different electrolyte and clay concentrations. Discrimination between gel and glass for the present system is beyond the scope of the present work.

When the samples are put between crossed polarizers, one can easily observe a birefringent phase. Figure 2(c) clearly displays the birefringency of the nematic phase.

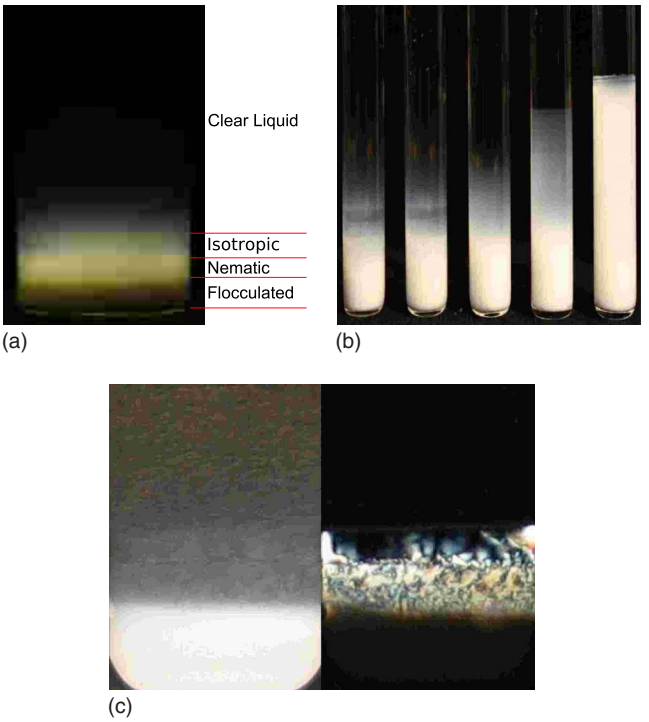


FIG. 2. (Color online) Samples: $H_2O$+NaCl+NaFHT after settling under action of gravity. All studied samples are 3% NaFHT by mass. (a) Four phases coexisting (different strata) in a single sample tube (circular ∅3 cm). 1 m*M* NaCl. (b) Effect of different salt concentrations (circular sample tube ∅1 cm). The amount of electrolyte has a significant effect on the system. NaCl concentrations from left to right: 0.1, 0.5, 1, 5, and 10 m*M*. (c) Birefringence of the nematic phase. Left: sample with black paper behind (its texture is seen). Right: sample between crossed polarizers. From bottom to top: opaque sediment, birefringent nematic, black isotropic with dendrites from nematic, and clear liquid separated by a thin line from isotropic (rectangular sample tube $1\times10$ mm$^2$).

The samples were brought to the Dutch-Belgian beamline (DUBBLE) at the European Synchrotron Radiation Facility (ESRF) 28 days before the date assigned for beam time, and they were left to rest there until the SAXS experiment was performed on site. The setup used covered the $q$ range $0.015<q<0.33$ nm$^{-1}$ [$q=|\mathbf{q}|=(4\pi/\lambda)\sin\theta$, where $\lambda$ is the x-ray wavelength and $2\theta$ is the scattering angle]; hence, the studied spatial resolution was approximately $2/q=10-130$ nm. Therefore, only the thickness of the aggregated particles and the expected interspacing can exhibit a signature in the data. The lateral size of these particles is generally too large to be seen here. By collecting two-dimensional (2D) data, we are able to distinguish standing aggregates from the ones that lie horizontally, and hence parallel arrangements from staggered ones.

Vertical transmission scans were performed for each sample, followed by data collection of SAXS patterns at different heights, from 1 up to 23 mm above the bottom of the sample. The clear liquid phase is located higher than that for all samples, and it was not studied here. Examples of patterns collected in the nematic and isotropic phases are displayed in Fig. 3; it is clear that the patterns are quite different

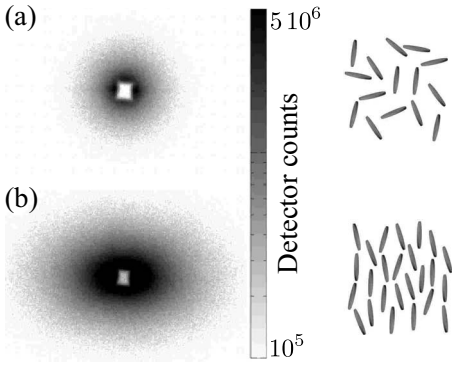


FIG. 3. Typical scattering patterns obtained in the experiment in (a) isotropic and (b) nematic phase. The sets of thin disks (viewed from the side) on the right exemplify possible arrangements responsible for creating the scattering patterns on the left.

from one phase to the other. In the isotropic gel the isointensity lines are circles; for the nematic gel they are ellipses with high eccentricity.

After the end of the experiment the patterns and the transmission data were carefully data reduced. The empty capillary scattering was not subtracted from the SAXS patterns since its scattering proved to be negligible compared to the scattering from the samples, but the empty tube absorption was taken into account in order to data-reduce the transmission data.

## III. DATA ANALYSIS AND DISCUSSION

### A. Phase diagram

In order to characterize the various phases, we determine isointensity lines of the SAXS patterns. For instance, if we select an intensity of around $2\times10^6$ detector counts, we have a circle in Fig. 3(a) and an ellipse for Fig. 3(b). In order to automate this analysis MATLAB was used to open each pattern, take a thin slice in intensity, and fit an ellipse to it. From this process, values for the semiaxes $a$ and $b$ of the ellipse and its angle of tilt were obtained; more details on this procedure can be found in Ref. [11]. Tables for the eccentricity ($e=\sqrt{1-b^2/a^2}$) and the angle of tilt were then built. However, since the saline concentrations used in the experiment form a nonregularly and nonmonotonically spaced grid, they were rebinned in order to create color maps from these tables [Figs. 4(a)–4(c)]. Owing to the fact that the angle of tilt has little significance for low-eccentricity patterns (i.e., ellipses close to circles), the low-eccentricity ($e<0.5$) regions of Fig. 4(b) were whitened. Also, since we are interested only in how much the particle orientations deviate from the horizontal and vertical, the angle data were remapped from the interval (0,360]° to (0,90]°.

From Figs. 4(a) and 4(b), we can easily identify the borders of the phases. The identification of the isotropic and nematic gels is rather straightforward since the former is characterized by low eccentricities (the ellipses are almost circles), while the latter is characterized by high eccentricities and low angles of tilt (the ellipses are horizontal). The sediment and flocculated phase display from low to average

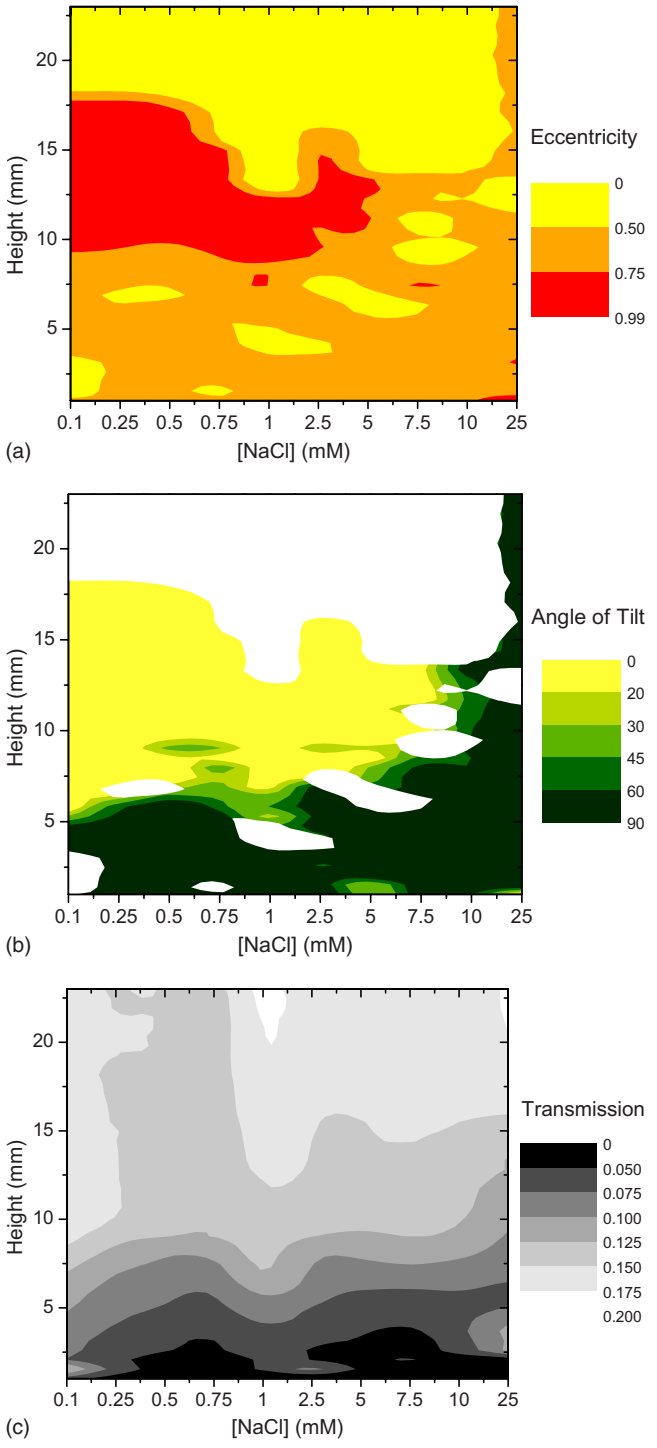


FIG. 4. (Color online) Color maps for the NaCl concentrations studied. The height above the bottom of the sample tube ranges from 1 up to 23 mm. (a) and (b) are constructed from analysis of the isointensity lines of the SAXS patterns. (a) Eccentricity. (b) Angle of tilt (low-eccentricity areas were whitened). (c) Transmission.

eccentricities and all possible angles of tilt, but on average they exhibit high angles of tilt (close to 90°). However, for higher saline concentrations, there is a change in behavior and, in the place where we would expect the nematic phase, higher angles of tilt are noticed; the eccentricities there are

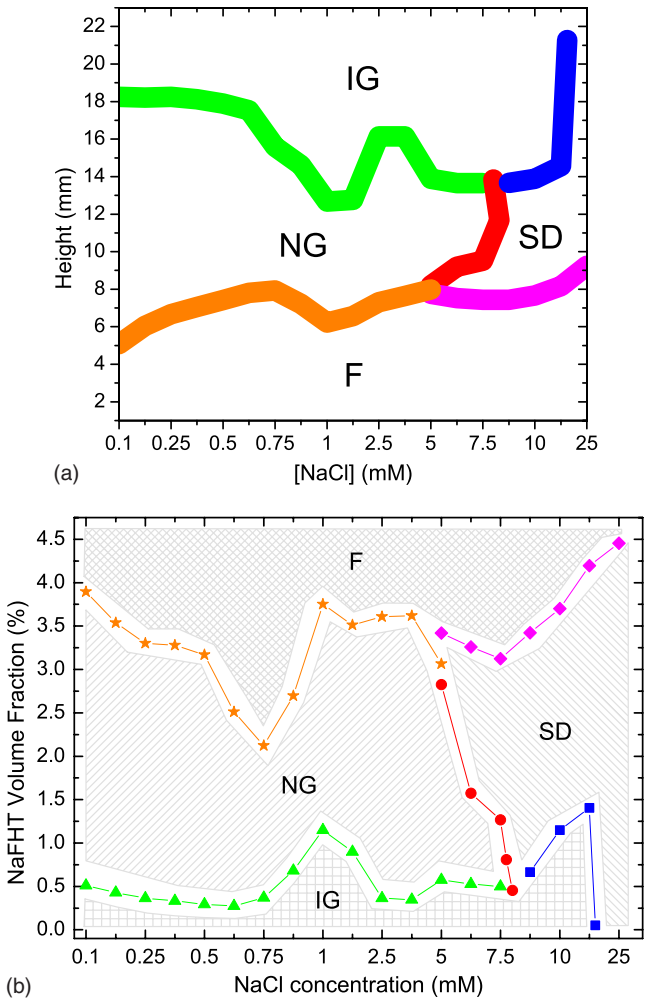


FIG. 5. (Color online) Phase borders for the samples. (a) Phase borders inferred from the eccentricity and angle of tilt color maps; see Figs. 4(a) and 4(b). (b) Phase diagram of the Na-fluorohectorite system, constructed from the phase borders of (a) and from the $z$ (height) to $\Phi$ (clay volume fraction) relation inferred from the transmission color map.

lower than in the nematic but higher than in the isotropic phase. Also, some of the SAXS patterns in this region seem to be the superposition of ellipses at different angles of tilt (hence the final eccentricity—as computed here—is lower than for the individual ellipses). This agrees with a previous suggestion [8] of small domains (SDs) for those saline concentrations. Lastly, in order to separate the SDs from the sediment we assumed that the transmission values that separated sediment from nematic ($T \approx 0.1$) are still the threshold. The identified borders were put together in Fig. 5(a).

The next step is to go from the phase borders to a proper phase diagram, i.e., instead of using the height above the sample bottom $z$, we employ an intensive parameter, in the present case the clay volume fraction $\Phi$, which is known from previous works on similar systems [18], and for nematically ordered systems in general from as early as the Onsager theory [15], to be a potential control parameter for the isotropic-nematic transition. In order to determine its values we used the transmission data, starting by assuring that the data were properly reduced, i.e., the transmission comes only from the sample (no glass). The transmission is given by

$$T = \exp(-\mu\rho d), \tag{1}$$

where $\mu$ is the mass absorption cross coefficient, $\rho$ is the material density, and $d$ is the thickness of the sample. Also, the linear absorption coefficient is defined as $\alpha \equiv \mu\rho$.

The x rays illuminate a volume $V=Ad$, where $A$ is the section of the incoming beam, and $d$ is the diameter of the tube (if the beam is well centered on the tube). In case the probed volume is much greater than the volume of the particles, as it is in the present case, we can write

$$\alpha = \frac{\alpha_c V_c + \alpha_s (V - V_c)}{V}, \tag{2}$$

where $\alpha_c$ and $\alpha_s$ are the absorption coefficients for the clay and the solution, respectively, and $V_c$ is the total volume occupied by the clay particles in the probed volume. Using Eq. (1), Eq. (2) becomes

$$\frac{1}{d} \ln T = -\frac{\alpha_c V_c + \alpha_s (V - V_c)}{V}. \tag{3}$$

We now note that the volume fraction of clay is given by

$$\Phi = \frac{V_c}{V}. \tag{4}$$

Putting together Eqs. (3) and (4) we obtain

$$\Phi = -\frac{(1/d)\ln T + \alpha_s}{\alpha_c - \alpha_s}. \tag{5}$$

In Eq. (5), $T$ was measured in the experiment, $d$ is known, and the values for $\alpha_s$ and $\alpha_c$ can be determined theoretically as follows. Knowing the energy of the x rays (7.999 keV) one can evaluate the scattering cross section for each element [19]. From the knowledge of the chemical formula, the cross sections for the elements are weight averaged in order to obtain the cross section for the components of our samples (see Table I). Here the cross section is the sum of both photoabsorption and inelastic scattering cross sections, since we have light elements. Also, it is worth noting that the energy employed is far from absorption edges. Using the values from Table I and the mass density, one can find the corresponding linear absorption coefficients (see Table II).

The conversion from the $([\mathrm{NaCl}], z)$ to the $([\mathrm{NaCl}], \Phi)$ coordinate system is done in practice in the following way. From Eq. (5) and Tables I and II, a $\Phi([\mathrm{NaCl}], z)$ color map is plotted (not shown here), and the borders from Fig. 5(a) are superimposed on this plot. Then, the values of the clay volume fraction along the borders are collected. The phase diagram for the system is created by plotting these values versus salt concentration, as shown in Fig. 5(b). Note that the clear liquid phase was not studied and therefore its border is not presented here, and that for the highest saline concentration the isotropic phase starts higher than the studied range; thus it is not shown in the figure. Note that this approach is not completely sound for measurements performed too close to the bottom of the sample, since the diameter of the capillaries usually varies there.

TABLE I. Calculated cross sections.

| Element | Atomic weight (g/mol) | Relative weight | Cross section ($cm^2/g$) | Weighted cross section ($cm^2/g$) |
|---|---|---|---|---|
| | | NaCl | | |
| $1\times$Na | 22.99 | 0.39 | 28.42 | 11.178 |
| $1\times$Cl | 35.45 | 0.61 | 104.89 | 63.629 |
| Total | 58.44 | | | 74.807 |
| | | NaFHT | | |
| $0.6\times$Na | 13.79 | 0.04 | 28.42 | 1.014 |
| $2.4\times$Mg | 58.33 | 0.15 | 39.79 | 6.003 |
| $0.6\times$Li | 4.16 | 0.01 | 0.37 | 0.004 |
| $4\times$Si | 112.34 | 0.29 | 61.67 | 17.919 |
| $10\times$O | 159.99 | 0.41 | 11.35 | 4.696 |
| $2\times$F | 38 | 0.1 | 15.52 | 1.525 |
| Total | 386.62 | | | 31.160 |
| | | $H_2O$ | | |
| $2\times$H | 2.02 | 0.11 | 0.35 | 0.040 |
| $1\times$O | 16 | 0.89 | 11.35 | 10.078 |
| Total | 18.02 | | | 10.118 |

First, it does not show a columnar phase owing to the high polydispersity of the system [16,17]; this was corroborated by thorough visual observations (shining visible light on the samples would produce bright reflections if there were columnar phases present). Second, we observe that in the low NaCl range (up to 0.75 m*M*), an increase in saline or particle concentration favors flocculation regarding the nematic gel (NG)-flocculated (F) transition; and favors the nematic phase in the isotropic gel (IG)–NG case. Both cases were expected since, as more particles are added, making them approach each other more closely, excluded volume effects tend to favor particle alignment (hence, the nematic phase); furthermore, an increased screening of their charges through addition of electrolyte leads to a decrease of the particles' electric diffuse layer volume, and therefore to the same result. As the particle or saline concentration is further increased it leads to flocculation of the particles.

From 1 to 2.5 m*M* there seems to be a discontinuity in the behavior at the left and at the right of this region. This is not unexpected since sudden changes in sample behavior have been seen to occur for saline concentrations around 1 m*M* for this system.

In the range from 2.5 m*M* and higher we notice that as the NaCl amount is increased the small-domain phase appears. At the highest saline concentration studied, i.e., 25 m*M*, the phase diagram shows that the flocculated and nematic phases seem to have merged into a single phase which goes higher in the sample tube. Visual observation of the sample does not

TABLE II. Cross sections for the compounds of interest at 20 °C and for a wavelength of 1.55 Å.

| Compound material | $\rho$ ($g/cm^3$) | $\mu$ ($cm^2/g$) | $\alpha$ ($cm^{-1}$) |
|---|---|---|---|
| $Na_{0.6}(Mg_{2.4}Li_{0.6})\ Si_4O_{10}F_2$ | 2.75 | 31.160 | 85.69 |
| $H_2O$ | 0.9982 | 10.118 | 10.100 |
| NaCl | 2.16 | 74.807 | 161.583 |
| 0.1 m*M* NaCl | 0.99824 | 10.118 | 10.100 |
| 0.25 m*M* NaCl | 0.99825 | 10.119 | 10.101 |
| 0.5 m*M* NaCl | 0.99826 | 10.120 | 10.102 |
| 0.75 m*M* NaCl | 0.99827 | 10.121 | 10.103 |
| 1 m*M* NaCl | 0.99828 | 10.122 | 10.104 |
| 2.5 m*M* NaCl | 0.99834 | 10.127 | 10.111 |
| 5 m*M* NaCl | 0.99844 | 10.137 | 10.121 |
| 7.5 m*M* NaCl | 0.99855 | 10.146 | 10.132 |
| 10 m*M* NaCl | 0.99865 | 10.156 | 10.142 |
| 25 m*M* NaCl | 0.99927 | 10.212 | 10.205 |

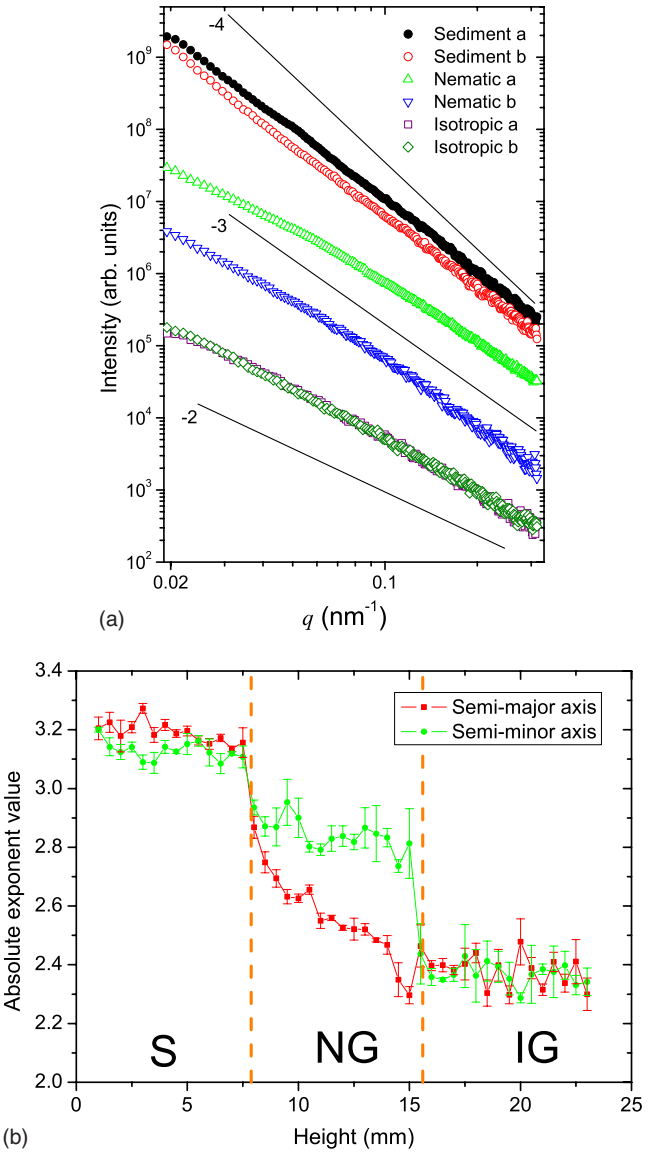


FIG. 6. (Color online) Scattering along the semimajor and semiminor axes for 0.75 m$M$ NaCl sample. (a) Power-law behavior along the semiaxes $a$ (major) and $b$ (minor) in the sediment (vertically displaced by 10), nematic (no displacement), and isotropic (displaced by $10^{-1}$) phases. (b) Exponent values in the high-$q$ range versus height in sample. There is a clear split in values in the nematic phase and a small one in the sediment.

reveal a dividing line between the nematic and flocculated phases as the other samples do.

One possible interpretation for the observed behavior in the phase diagram is that we have both gel formation at lower saline concentrations (NG below 1 m$M$) and glass formation at higher concentrations (NG above 1 m$M$), similar to what was recently observed for laponite [20]. A comparison between gel and glass can be found in Ref. [21]. Hence, we suggest that the region around 1 m$M$ could be a transition region between both arrested states of matter. In this picture, a further increase in saline concentration leads to glass formation at high NaCl concentration (around 25 m$M$).

In addition, our diagram displays a reentrant behavior reminiscent of that observed in laponite by Levitz *et al.* [22]:

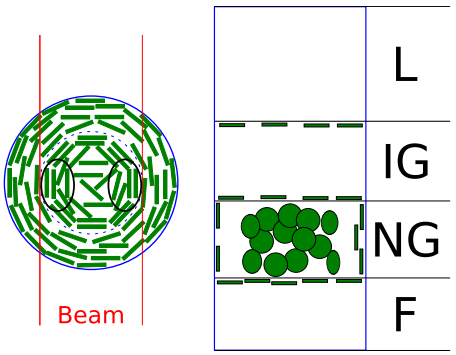


FIG. 7. (Color online) Organization of the platelets in the nematic phase and close to the phase borders. The disproportional image on the left is a section through the nematic phase. In the NG phase the particles contributing to the anisotropic scattering are mostly located between the particles close to the wall and those in the center (see the regions denoted by the two ellipses), and they must have their diameters along the beam path.

by following a line at constant particle volume fraction close to 1% in the phase diagram in Fig. 5(b), as the salt content is increased, one goes from the nematic gel to the isotropic gel and then back to the nematic gel; the same is observed between the nematic gel and the flocculated phase at particle volume fractions between 2% and 3.5%. In the study by Levitz *et al.*, the reentrant behavior involved two solidlike phases separated by the liquid phase, with a characteristic ionic strength of 0.1 m$M$ separating a region of high ionic strength in which the Debye screening length was smaller than the diameter of laponite particles (approximately 30 nm), and another one in which their behavior was that of soft repulsive spheres due to the screening length being larger than the particle diameter. In our study, however, the screening length is always significantly smaller than the typical fluorohectorite particle diameter. Therefore, the reentrant behavior that we observe does not necessarily have the same origin as that mentioned in Ref. [22].

Further studies are needed to understand the phases present in the diagram. Cryofracture could possibly elucidate how the particles are organized in each phase, and provide additional information about the particle distribution size at each phase.

### B. Radial intensity decays

When considering the radial decay of the scattering images, we notice that our system displays power-law behavior, i.e., $I(q) \propto q^{-\kappa}$. We have analyzed profiles of the scattering intensity $I(q)$ as a function of the magnitude of the scattering vector $q$ along the semiaxes of the ellipse. Typical profiles for the three studied phases are exemplified in Fig. 6, where the plots regarding the sediment have been translated vertically by a factor of 10 whereas the ones for the isotropic phase have been displaced by a factor of 0.1. The profiles obtained do not present any peaks, indicating the lack of positional ordering within this $q$-range.

The scattering patterns displayed in Fig. 6 show shoulders around $q_c = 0.05 - 0.06$ nm$^{-1}$; thus for a value of $1/q_c$ around

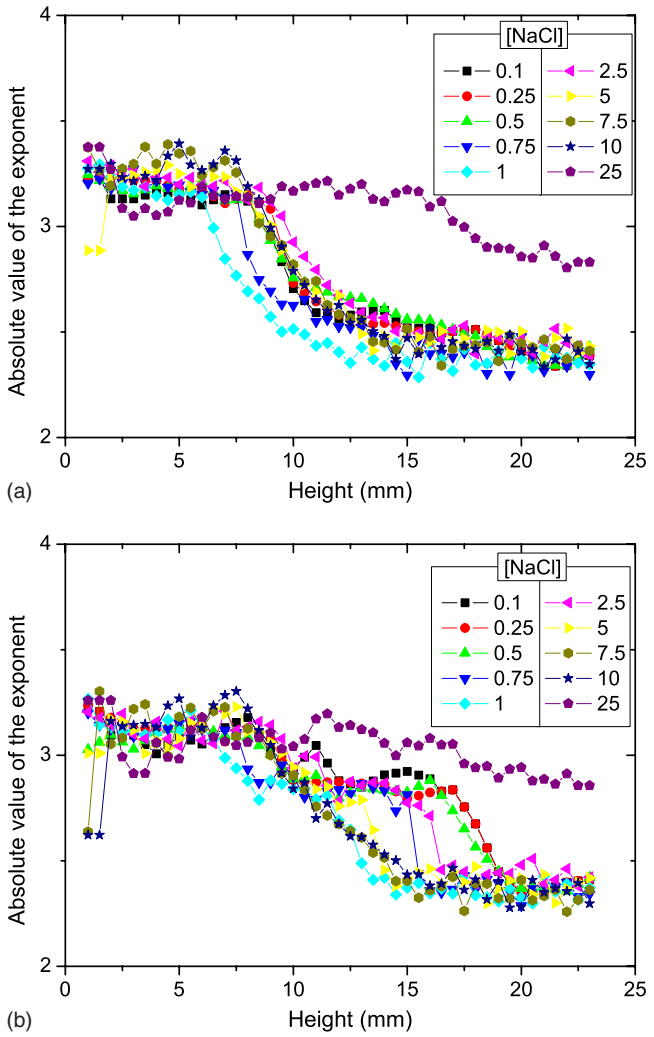


FIG. 8. (Color online) Absolute values of the exponents in the high-$q$ range for the studied NaCl concentrations. The behavior at 25 m$M$ NaCl is clearly different from that of the other saline concentrations. (a) Semimajor axis. For saline concentrations 0.1–10 m$M$ all samples are similar with the exception of 0.75 and 1 m$M$, which are in a discontinuity region from the gel to the glass. (b) Semiminor axis. Some of the saline concentrations now exhibit a step.

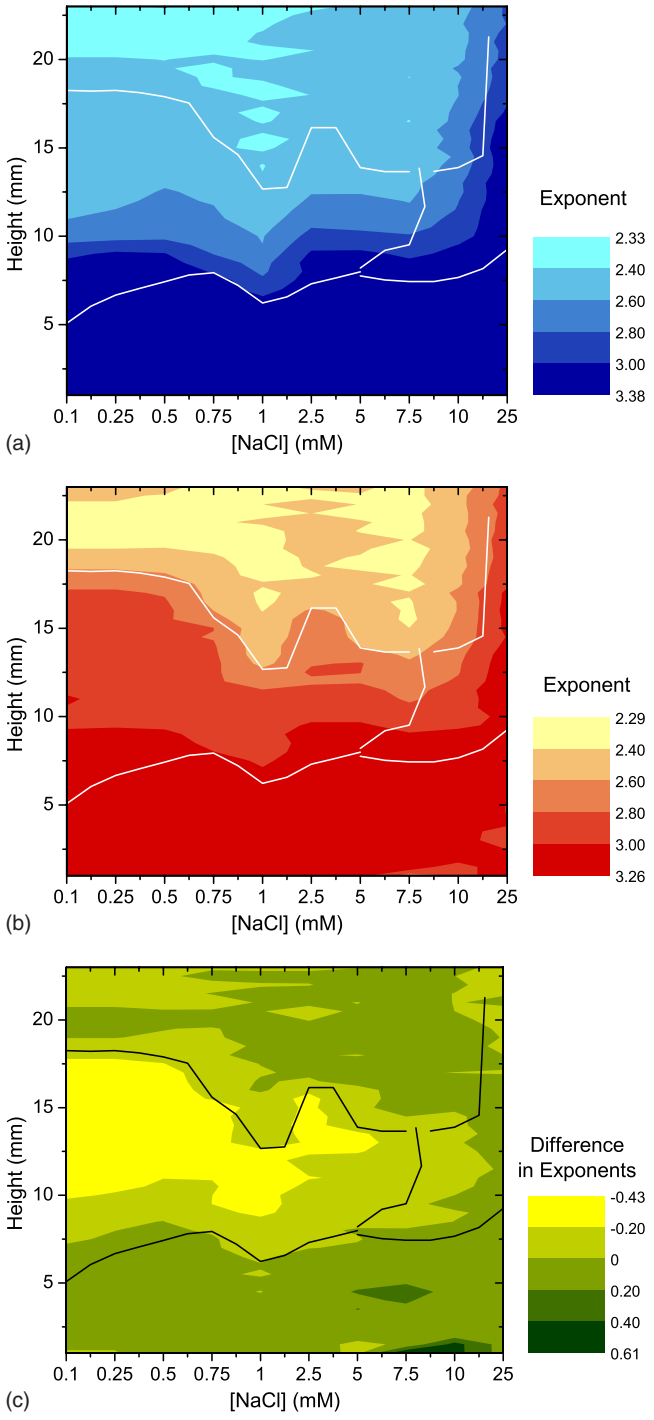


FIG. 9. (Color online) Color maps for the absolute values of the exponents in the high-$q$ range. (a) Semimajor and (b) semiminor axis. (c) Difference between (a) and (b). The largest differences occur in the zone corresponding to the nematic phase. We observe that (a) displays steeper exponents in the sediment, whereas (b) displays steeper exponents in the nematic phase. The phase boundaries from Fig. 5(b) are superimposed onto the maps.

20 nm. However, in the present case, with a system of thin platelets, the relevant crossover length is $2/q_c$, as shown in Fig. 13(a) in the Appendix. Thus we observe a characteristic average dimension of about 36 nm for the particles in our system. The shoulder is seen most clearly for the nematic phase, but is present for all studied phases. It must therefore correspond to some dimension present in all phases; hence it is most likely related to the average platelet thickness in our system. We discuss now the exponents for the high-$q$ range, defined here as those where $q > 0.06$ nm$^{-1}$.

In Fig. 6(b) we notice that the exponents drop from −3.2 in the sediment to −2.4 in the isotropic phase. It is interesting to note that the two axes change differently within the nematic phase. For the semiminor axis the slope just decreases in one step to −2.8. However, for the semimajor axis it initially drops to −2.8 and then linearly decreases to −2.4. Owing to the polydispersity of the system and also to the particle interactions we can only attempt a qualitative analysis. We know (see the Appendix) that for highly ordered disks the decay in scattered intensity corresponds to an exponent −3 for scattering vector perpendicular to the normal of the disk.

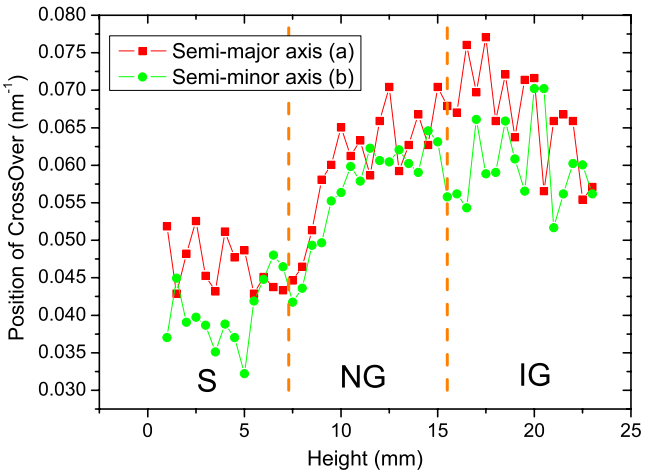


FIG. 10. (Color online) Crossover positions for the 2.5 m$M$ NaCl sample.

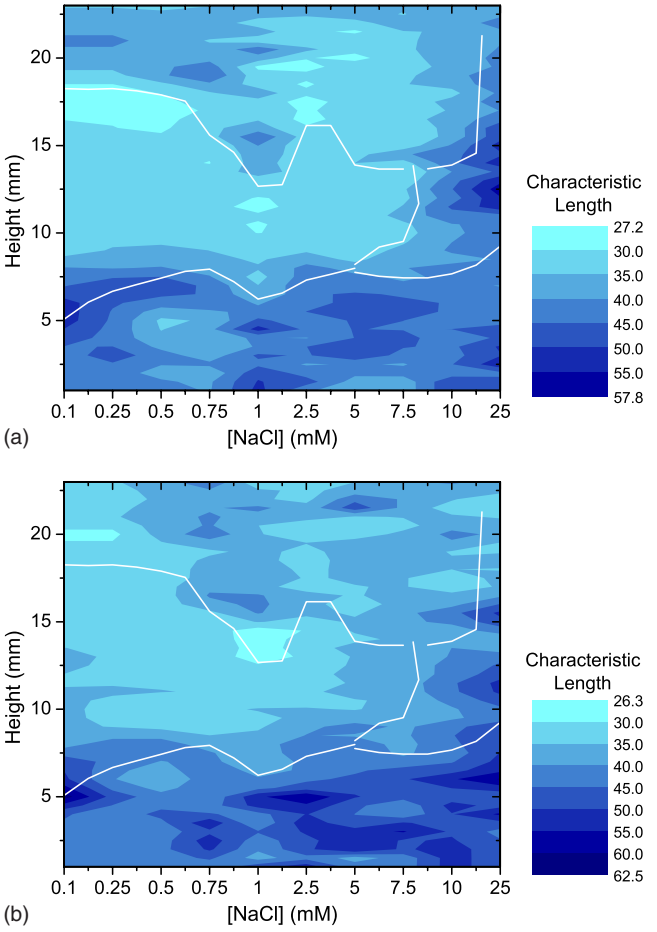


FIG. 11. (Color online) Color map for the corresponding characteristic lengths for the crossover positions. The phase boundaries from Fig. 5(b) are superimposed onto the map. (a) Semimajor axis and (b) semiminor axis.

On the other hand, for such systems, along the direction where the scattering vector is parallel to the normal the power law has an exponent of −2. Hence, from Fig. 6(b) we can infer qualitatively how the platelets are oriented in the nematic phase, since the ellipse tilt is 0° and since along the semiminor axis we observe an exponent close to −3 whereas for the semimajor axis it is around −2. This together with information from MRI results in Ref. [10] allows us to draw Fig. 7. From the MRI data one can also conclude that we should not expect values of exactly −3 and −2, since the particles with their normal parallel to the beam (like those close to the wall) contribute to decreasing the higher exponent and increasing the lower one. Note, however, that the sample cell used here has a diameter of 2 mm whereas for the one in Ref. [10] it is 10 mm. And in their case of wider cells, the authors of [10] observed that the orientational ordering occurs only close to the glass walls.

Here, since the sample tube is narrow, frustration occurs in its center, leading to a nematic phase with a line defect disclination of strength $m=+1$ [23–25] and if the diameter of the sample tube was increased the bulk would become isotropic, though the platelets close to the glass wall would still be oriented. A similar thought process regarding the moderate split in power-law exponents can be used for the sediment. In that case the populations of standing and lying particles are similar in number (the splitting is small), but the higher number of lying platelets is responsible for the observed eccentricity.

The orientation angles at the sediment (closer to 90°) are in agreement with those of Azevedo *et al.* [10], which concluded that at the transition from the nematic to the isotropic phase (isotropic in terms of water movement), the platelets below and above the boundary are edge to face. This observation is also in line with what was seen in Ref. [26].

In Fig. 8 we have plotted the evolution of the exponents along both semiaxes, for all samples. For the semimajor axis [Fig. 8(a)], all samples present the same behavior, with the exception of the highest saline concentration, namely, 25 m$M$, which behaves in a similar way along both axes, having a higher value than the others throughout. On the other hand, the semiminor axis [Fig. 8(b)] behaves differently. For the low saline concentrations, 0.1–2.5 m$M$, but not 1 m$M$, the decrease in exponent now exhibits a step, while for the rest of the concentrations the decrease now starts higher in the sample tube.

In Fig. 9, we have replotted the data from Fig. 8 as color maps. The difference between the two axes is plotted in Fig.

TABLE III. Expected power-law behavior.

| Noninteracting monodisperse disks | Low $q$ | Medium $q$ | High $q$ |
|---|---|---|---|
| Randomly oriented | | $q^{-2}$ | $q^{-4}$ |
| Highly oriented ($\mathbf{q}\perp\hat{\mathbf{n}}$) | | $q^{-3}$ | $q^{-3}$ |
| Highly oriented ($\mathbf{q}\parallel\hat{\mathbf{n}}$) | | | $q^{-2}$ |

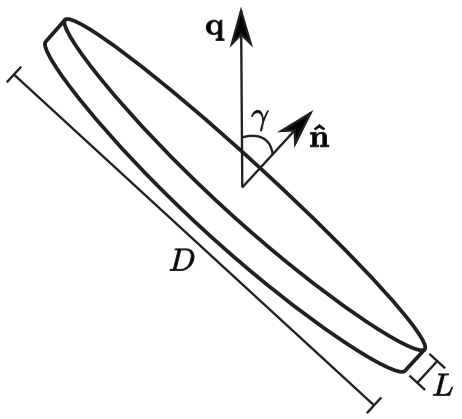


FIG. 12. Platelet geometry.

9(c), from which it is very clear that most of the difference in behavior occurs in the nematic phase, where the absolute value of the exponents is higher for the semiminor axis.

In Fig. 10, the position of the crossover in the SAXS data has been plotted. The characteristic length—inversely proportional to the position of the crossover—indicates thicker clay particles in the sediment (as expected). The behavior along both axes is very similar, indicating that the absence of ordering in the center of the tube makes the projection of the diameter of the platelets visible along both axes, though weaker for $b$. If we convert the shoulder position to the characteristic length $2/q_c$, we note that in the sediment it has a value of around 43 nm for the $a$ axis and 50 nm for the $b$ axis, whereas for the isotropic phase they are respectively equal to 30 and 33 nm. These values are within the range found in Ref. [8].

We have plotted the characteristic lengths for the crossover positions as color maps in Fig. 11. The plots suggest that particles are thicker in the floculated or sediment phase, but that they have similar thicknesses in both isotropic and nematic gels.

## IV. CONCLUSION

We employed SAXS to determine the proper phase diagram for the NaFHT-NaCl-$H_2O$ system, for which all gel or glass phases are visible simultaneously in each sample tube. The high polydispersity and the interaction of the particles did not allow us to fully understand the structural arrangement in the different phases. In particular, we believe that there are different arrested states (gel and glass phases) in the phase diagram, and further investigation is needed to corroborate that. However, we believe that the physical mechanism leading to the formation of these coexisting phases is to be understood as follows. It is driven by the sedimentation: after the flocculated phase has been formed by sedimentation of aggregates of clay particles and of the largest particles, further sedimentation of non-Brownian (large) clay particles occurs, leading to a vertical gradient in particle volume fraction. We have estimated this vertical volume fraction profile from x-ray absorption data. This eventually leads to nematic ordering in the lower (and denser) region above the flocculated phase, until the whole structure is "frozen" by gelation (or glass formation) over time. If the characteristic time for gelation were much smaller than that for the appearance of a nematic phase by sedimentation, we would see no appearance of a nematic gel phase within time scales of the order of our current observation time (i.e., some weeks).

The use of a 2D detector and analysis of the data along the two semiaxes proved useful in determining the orientational configuration of the platelets in the nematic phase and to some extent in the flocculated phase. However, the different particle configurations made it impossible to completely decouple the optical axes of the particles. A new experiment using narrow rectangular-section cells instead of circular ones will probably allow even more information to be extracted from the scattering intensity curves. However, by comparing the results from Ref. [10] to our observations, we were able to determine a plausible collective organization of the particles in the nematic phase. For future studies, we believe that a thorough cryofracture study of the phase diagram would determine the conformation of the particles in all phases, and would provide information on the particle-size distributions as a function of height in the sample tube.

In terms of particle typical sizes, we were able to draw the following conclusions. Particles in the nematic and isotropic phases were observed to have similar thickness, whereas the flocculated phase presents thicker particles. The particles in the nematic phase have their edges close to the glass walls of the tube and the platelets are standing (their normal is perpendicular to the tube axis). Particles in the flocculated phase have an almost isotropic distribution of orientations when compared to the nematic phase, but a slightly higher number of platelets lie horizontally.

## ACKNOWLEDGMENTS

The authors acknowledge the European Synchrotron Radiation Facility for provision of synchrotron radiation facilities and we would like to thank Dr. Igor Dolbnya for assistance in using beamline BM26B. This work has received partial financial support from the Research Council of Norway (RCN) through the NANOMAT Program, RCN Projects No. 152426/431, No. 154059/420, and No. 148865/432, as well as through Projects No. 138368/V30 and No. SUP154059/420. Y.M. acknowledges travel support from the Egide organization under the Aurora project for French-Norwegian collaboration.

## APPENDIX: POWER-LAW DECAY IN MODEL PLATELET SYSTEMS

The form factor $P(q)$ for a cylinder of diameter $D$ and thickness $L$ is given by [27]

$$P(q,\gamma) = \rho V \frac{\sin w}{w} \frac{2J_1(x)}{x}, \tag{A1}$$

where

$$w = qL \cos \gamma/2 \tag{A2}$$

and

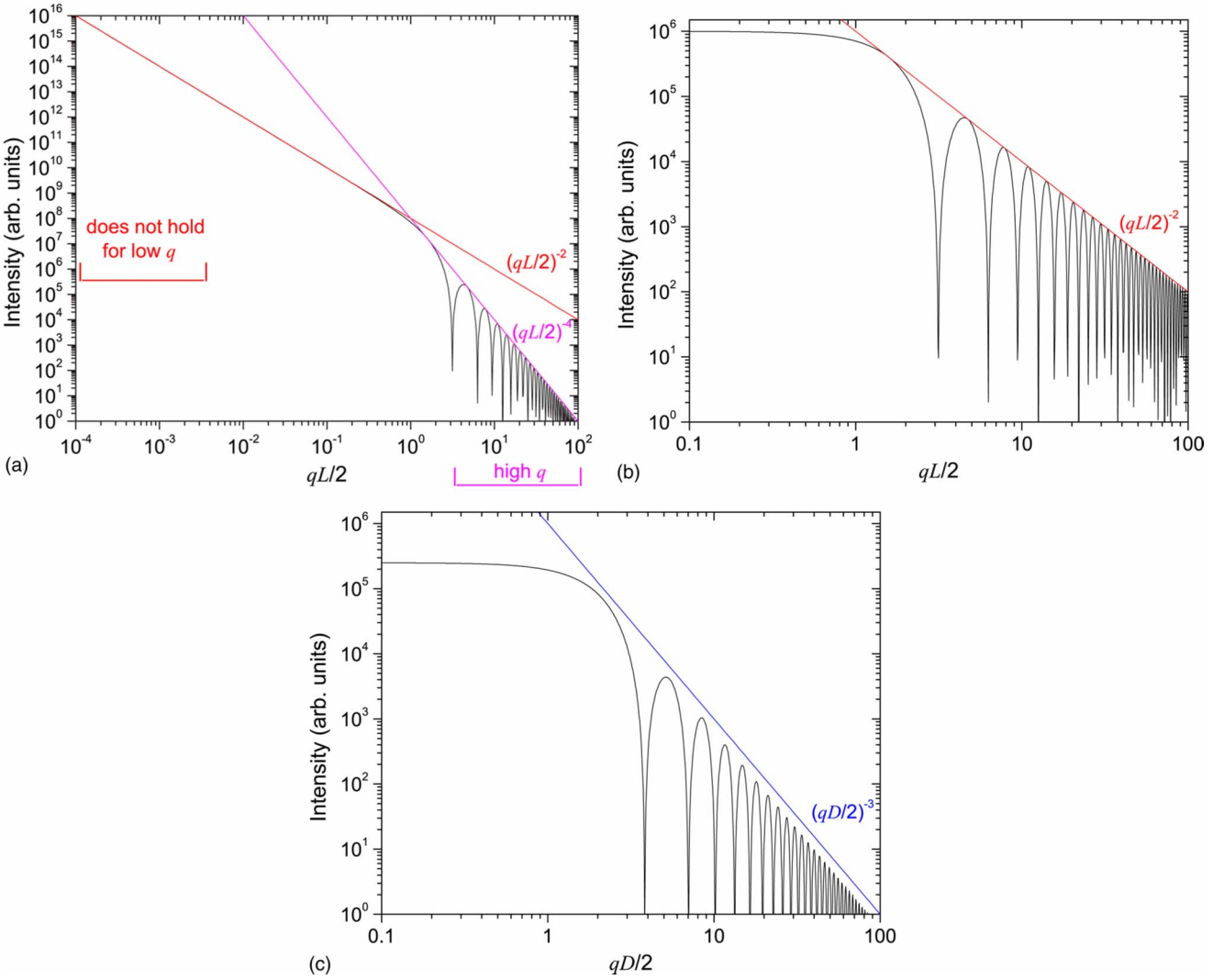


FIG. 13. (Color online) Expected power-law behavior for noninteracting monodisperse platelets. (a) Randomly oriented platelets case. A crossover is observed at $q \approx 2/L$. (b) Highly oriented platelets, parallel case ($\mathbf{q} \| \hat{\mathbf{n}}$). Note the shoulder at $q \approx 3/L$. (c) Highly oriented platelets, perpendicular case ($\mathbf{q} \perp \hat{\mathbf{n}}$). A shoulder occurs at $q \approx 4/D$.

$$x = q\frac{D}{2}\sin\gamma. \tag{A3}$$

Here $\gamma$ is the angle between $\mathbf{q}$ and the normal of the disk, $\hat{\mathbf{n}}$ (see Fig. 12), $V$ is its volume, $\rho$ is the electronic density difference between the particle and the medium, and $J_1$ denotes the first-order Bessel function of the first kind.

For simplicity's sake we will assume that the particles do not interact; hence the structure factor will be neglected, i.e., $S(q)=1$. Also, we assume that the disks are monodisperse. In this case the scattered intensity for an isotropic system is

$$I(q) = K\langle |P(q)|^2 \rangle_\gamma, \tag{A4}$$

where $K$ is an experimental constant and $\langle\ \rangle_\gamma$ should be understood as an average over all orientations.

Following the results obtained in Ref. [28] for isotropic and oriented systems of platelets, we note that for thin platelets ($D \gg L$) the term in $x$ in Eq. (A1) falls off much faster than the one in $w$. Hence only small $x$ values will contribute to the average, i.e., $x$ values for which $\mathbf{q} \perp \hat{\mathbf{n}}$. Thus Eq. (A4) can be approximated to

$$I(q)_{\text{isotropic}} \approx KA\frac{2\pi}{q^2}\left(\frac{\sin(qL/2)}{qL/2}\right)^2. \tag{A5}$$

Thus, the scattering intensity obeys a $q^{-2}$ power law, and in the limit of high $q$ it changes to a $q^{-4}$ power law. However, Eq. (A5) is not valid at low $q$ since in that case $x$ becomes significant.

On the other hand, for highly oriented systems we can divide the observed behavior into two cases, namely, transferred momentum along the normal of the platelet and perpendicular to it. In the former case, only the dependence on the thickness of the particle will survive; hence

$$I(q,\gamma=0)_{\text{oriented}} = K\left(\rho V \frac{\sin(qL/2)}{qL/2}\right)^2. \quad \text{(A6)}$$

For the latter case we note the opposite; thus only dependence on the particle diameter contributes,

$$I(q,\gamma=\pi/2)_{\text{oriented}} = K\left(2\rho V \frac{J_1(qD/2)}{qD/2}\right)^2. \quad \text{(A7)}$$

Equations (A5)–(A7) are plotted in Fig. 13, where the power-law behavior for this model platelet system can be seen. From them we note that a crossover for randomly oriented disks occurs at $q \approx 2/L$, and that for oriented platelets with normal perpendicular (parallel) to the scattering vector a shoulder appears at $q \approx 4/D$ ($q \approx 3/L$). Also, we observe the modulation arising from $J_1(x)$ and $\sin w$. The expected power-law behaviors are summarized in Table III.


[1] *Handbook of Clay Science*, edited by F. Bergaya, B. K. Theng, and G. Lagaly (Elsevier, Amsterdam, 2006).
[2] G. J. da Silva, J. O. Fossum, E. DiMasi, K. J. Måløy, and S. B. Lutnæs, Phys. Rev. E **66**, 011303 (2002).
[3] A. Mourchid, E. Lécolier, H. Van Damme, and P. Levitz, Langmuir **14**, 4718 (1998).
[4] D. Bonn, H. Tanaka, H. Kellay, G. Wegdam, and J. Meunier, Langmuir **15**, 7534 (1999).
[5] B. J. Lemaire, P. Panine, J. C. P. Gabriel, and P. Davidson, Europhys. Lett. **59**, 55 (2002).
[6] A. Mourchid, A. Delville, J. Lambard, E. Lécolier, and P. Levitz, Langmuir **11**, 1942 (1995).
[7] P. D. Kaviratna, T. J. Pinnavaia, and P. A. Schroeder, J. Phys. Chem. Solids **57**, 1897 (1996).
[8] E. DiMasi, J. O. Fossum, T. Gog, and C. Venkataraman, Phys. Rev. E **64**, 061704 (2001).
[9] J. O. Fossum, E. Gudding, D. d. M. Fonseca, Y. Meheust, E. DiMasi, T. Gog, and C. Venkataraman, Energy **30**, 873 (2005).
[10] E. N. de Azevedo, E. Engesberg, J. O. Fossum, and R. E. de Souza, Langmuir **23**, 5100 (2007).
[11] D. M. Fonseca, Y. Méheust, J. O. Fossum, K. D. Knudsen, K. J. Måløy, and K. P. S. Parmar, J. Appl. Crystallogr. **40**, s292 (2007).
[12] M. B. McBride and P. Baveye, Soil Sci. Soc. Am. J. **66**, 1207 (2002).
[13] J. N. Israelachvili, *Intermolecular and Surface Forces*, 2nd ed. (Academic Press, London, 1992).
[14] D. van der Beek, Ph.D. thesis, Utrecht University, 2005.
[15] L. Onsager, Ann. N.Y. Acad. Sci. **51**, 627 (1949).
[16] F. M. van der Kooij, K. Kassapidou, and H. N. W. Lekkerkerker, Nature (London) **406**, 868 (2000).
[17] D. van der Beek, P. Davidson, H. H. Wensink, G. J. Vroege, and H. N. W. Lekkerkerker, Phys. Rev. E **77**, 031708 (2008).
[18] P. Davidson and J.-C. P. Gabriel, *Nanocrystals Forming Mesoscopic Structures* (Wiley-VCH, Weinheim, 2005), Chap. 7, pp. 173–212.
[19] http://henke.lbl.gov/optical_constants/pert_form.html
[20] B. Ruzicka, L. Zulian, R. Angelini, M. Sztucki, A. Moussaïd, and G. Ruocco, Phys. Rev. E **77**, 020402(R) (2008).
[21] F. Sciortino, Eur. Phys. J. B **64**, 505 (2008).
[22] P. Levitz, E. Lecolier, A. Mourchid, A. Delville, and S. Lyonnard, Europhys. Lett. **49**, 672 (2000).
[23] N. D. Mermin, Rev. Mod. Phys. **51**, 591 (1979).
[24] R. Repnik, L. Mathelitsch, M. Svetec, and S. Kralj, Eur. J. Phys. **24**, 481 (2003).
[25] P. G. de Gennes and J. Prost, *The Physics of Liquid Crystals*, 2nd ed., International Series of Monographs on Physics No. 83 (Clarendon Press, Oxford, 1993).
[26] M. Dijkstra, J.-P. Hansen, and P. A. Madden, Phys. Rev. E **55**, 3044 (1997).
[27] A. Guinier and G. Fournet, *Small Angle Scattering of X-Rays* (Wiley, New York, 1955).
[28] J. D. F. Ramsay, S. W. Swanton, and J. Bunce, J. Chem. Soc., Faraday Trans. **86**, 3919 (1990).